12th International Symposium on Turbulence and Shear Flow Phenomena (TSFP12)
Osaka, Japan, July 19–22, 2022

DIRECT NUMERICAL SIMULATIONS OF TURBULENT AIR INTAKE IN A HYPERSONIC FLOW

Youcheng Xi
School of Aerospace Engineering
Tsinghua University
Beijing, China, 100084
xiyc@mail.tsinghua.edu.cn

Song Fu
School of Aerospace Engineering
Tsinghua University
Beijing, China, 100084
fs-dem@tsinghua.edu.cn

ABSTRACT

In this study, the numerical simulations of turbulent flow in an air intake are performed to understand the characteristics of skin friction in hypersonic inner flows. A direct numerical simulation of a boundary layer is performed first to obtain turbulent information at the inlet of an intake, with the full process of transition and the growth of the boundary layer. Then the simulation of an air intake is undertaken. Integral analyses based on Cauchy's formula have been performed to reveal a detailed ingredients of skin-friction. It is found that the turbulence induced drag is the most dominant, in this case. The amplifications of turbulence is found after the interaction of the shockwaves and turbulent boundary layer, which lead to obvious increase of skin-friction. The results indicate that to reduced the drag in a hypersonic air intake, we need to impair turbulence.

1 Introduction

The hypersonic scramjet is considered to be one of the best propulsive choices for hypersonic flight(Urzay, 2018). Therefore, it is crucial to understand the aerodynamic behaviour for the device. Most air-breathing flights are designed as wave-rider, and the airflow is compressed dynamically through an intake system integrated with the fore-body. The flow is asked to become turbulent ahead of the combustion chamber in the air intake for the necessities of complete combustion. However, based on experimental studies, although the surface area of a scramjet combustion chamber only forms a small part, the high shear along its walls can account for more than half of the total engine skin-friction drag(Paull *et al.*, 1995; Robinson *et al.*, 2006). A reduction of the combustion chamber skin-friction drag therefore promises relatively large margins of performance improvement.

Therefore, it becomes a natural question before applying a method of drag reduction, what features does the flow have in the hypersonic air intake? In this research, direct numerical simulations, which provide a large amount of accurate data that can be used to analyse, are used to reveal the precise turbulent features in the hypersonic air intakes, focusing on the surface skin friction. Details of the numerical test case are described in Section 2. Results and some discussions are given in Section 3. The final conclusions are presented in Section 4.

2 Methodology

The governing equations for all simulations in this work are the dimensionless compressible Navier–Stokes equations for a Newtonian fluid, which can be written as:

$$\frac{\partial Q}{\partial t}+\frac{\partial F_j}{\partial x_j}+\frac{\partial F_j^v}{\partial x_j}=0, \tag{1}$$

$$Q=[\rho,\rho u_1,\rho u_2,\rho u_3,E_t]^T, \tag{2}$$

$$F_j=\begin{bmatrix}\rho u_j\\ \rho u_1u_j+p\delta_{1j}\\ \rho u_2u_j+p\delta_{2j}\\ \rho u_3u_j+p\delta_{3j}\\ (E_t+p)u_j\end{bmatrix},F_j^v=\begin{bmatrix}0\\ \tau_{1j}\\ \tau_{2j}\\ \tau_{3j}\\ \tau_{jk}u_k-q_j\end{bmatrix}. \tag{3}$$

Throughout this work the coordinates $x_i,(i=1,2,3)$ are referred to as x,y,z for the stream-wise, bottom wall-normal and spanwise directions, respectively, with corresponding velocity components u,v,w.

The total energy E_t and the viscous stress τ_{ij} are given as, respectively,

$$\begin{aligned}E_t&=\rho\left(\frac{T}{\gamma(\gamma-1)M_\infty^2}+\frac{u_ku_k}{2}\right),\\ \tau_{ij}&=\frac{\mu}{Re_\infty}\left(\frac{\partial u_i}{\partial x_j}+\frac{\partial u_j}{\partial x_i}-\frac{2}{3}\delta_{ij}\frac{\partial u_k}{\partial x_k}\right).\end{aligned} \tag{4}$$

The pressure p and heat flux q_i are obtained from:

$$p = \frac{\rho T}{\gamma M_\infty^2}, \quad q_i = -\frac{\mu}{(\gamma-1)M_\infty^2 Re_\infty Pr}\frac{\partial T}{\partial x_i}. \tag{5}$$

The viscosity is calculated using the Sutherland law

$$\mu = T^{3/2}(T_\infty + C)/(TT_\infty + C), \tag{6}$$

with $C = 110.4K$. The free-stream Reynolds number Re_∞, Mach number Ma_∞ and Prandtl number Pr are defined as

$$Re_\infty = \frac{\rho_\infty^* U_\infty^* l_0^*}{\mu_\infty^*}, \quad Ma_\infty = \frac{U_\infty^*}{\sqrt{\gamma R_g^* T_\infty^*}}, \quad Pr = 0.72, \tag{7}$$

where ρ_∞^*, U_∞^*, T_∞^* and μ_∞^* stand for the freestream density, velocity, temperature and viscosity, respectively. $R_g^* = 287J/(K \cdot Kg)$ represents the gas constant and γ stands for the ratio of specific heat. The length scale l_0^* is chosen as $1(mm)$ in this research.

The parallel computational code OPENCFD, developed by Li *et al.* (2008), has been used for the direct numerical simulation(DNS). The compressible Navier–Stokes equations are solved numerically using high-order finite-difference methods. Convection terms are discretized with Steger–Warming splitting and a seventh-order weighted essentially non-oscillatory scheme. Viscous terms are discretized with an eighth-order centred finite-difference scheme. A third-order total variation diminishing-type Runge–Kutta method is used for the time. Validations and verifications of the code can be found in a series of papers (Li *et al.* (2008); Liang *et al.* (2010); Li *et al.* (2010)).

The simulation processes are divided into three steps. At first, the simulation is conducted over a two-dimensional blunt plate with the high-order shock-fitting method(Xi *et al.*, 2021). During the two-dimensional analysis, the inlet profile of the boundary layer is obtained. Then, a transitional flat boundary layer is calculated with the computational domain inside the shock layer, with the inlet profile of the boundary layer. Wall blowing and suction perturbations are used to trigger the transition as soon as possible, with substantial amplitude. When the turbulent boundary layer is fully developed, the unsteady flow field at the specific stream-wise station ($x = 1400$) is recorded and used as inlet information for the Intake simulation. Finally, with the recorded turbulent information, a simulation of air intake is performed for investigation.

Table 1. Basic Parameters for simulations

Ma_∞	T_∞(K)	Re_∞	γ	Pr
4.8	1314	7123	1.4	0.72

Basic parameters for the present simulations are shown in Table 1. For both simulations, adiabatic surface boundary condition is assumed and periodic boundary conditions are used along the spanwise direction. Nonreflecting boundary condition is implemented on the outflow boundary along the stream-wise direction.

The computational domain, mesh number, and mesh resolution in wall unit are shown in Table 2 and 3. For the transitional boundary layer, 4482 grid points are used along the stream-wise direction. 140 grid points are used along the wall-normal direction and grid clustering is used to ensure at least 50 grid points are inside the boundary layer. The span-wise direction z is discretized by 256 grid points. For the turbulent air intake, 1551, 401 and 256 grid points are used along stream-wise, wall-normal and span-wise direction, respectively. Based on inner scale, the stream-wise grid space is $\delta x^+ = 6.35$ and 6.4. The wall-normal grid space for the first grid to the wall is unchanged in the whole domain, and $\delta y^+ = 0.47$ and 0.5. The wall-normal mesh is gradually coarsened away from wall surfaces. Due to the development of turbulence along the stream-wise direction, spanwise grid space is $\delta z^+ = 3.72$ in plate boundary layer, and is 4.5 in the intake.

Table 2. Summary of mesh resolution for numerical simulation of transitional boundary layer

Domain Size	x(m)	y(m)	z(m)	
	1.33	0.036	0.03	
Re_τ	$C_f \times 10^{-3}$	δx^+	δy^+	δz^+
$249-582$	1.3-1.1	6.35	0.47	3.72
Re_θ	Re_∞	N_x	N_y	N_z
$1424-5954$	7123	4482	140	256

Table 3. Summary of mesh resolution for the numerical simulation of intake

Domain Size	x(m)	y(m)	z(m)	
	0.3	0.024	0.03	
Re_τ^{in}	$C_f^{in} \times 10^{-3}$	δx^+	δy^+	δz^+
552	1.1	6.4	0.5	4.5
Re_θ	Re_∞	N_x	N_y	N_z
$4986-9715$	7.12×10^6	1551	401	256

3 Result and Discussion

The snapshots of vortices by sio-surface of the λ_2-criterion with $\lambda_2 = -0.05$ are shown in figure 1. The region $x \in [1000-1100]$ are enlarged on the bottom right. On the top left, the Reynolds- and spanwise-averaged van Driest velocity U_{VD}^+(Van Driest, 1951) profiles at $x = 1400$ is compared with theoretical results,

$$y^+ = \frac{\rho_w u_\tau y}{\mu_w}, u_{VD}^+ = \frac{u_{VD}}{u_\tau}, u_\tau = \sqrt{\frac{\tau_w}{\rho_w}}, u_{VD} = \int_0^u \sqrt{\frac{\rho}{\rho_w}} du, \tag{8}$$

where τ_w and ρ_w are the wall shear stress and surface density. As shown in the figure, the result agrees well with all the theoretical values in both the inner layer and the log layer, which indicate that the turbulent boundary layer is fully developed.

The snapshots for air intake of vortices by iso-surface of the λ_2-criterion with $\lambda_2 = -0.03$ are shown in figure 2. The Reynolds- and spanwise-averaged skin-friction coefficient C_f of the bottom is exhibited at the top left, where $C_f = 2\tau_w/\left(\rho_\infty^* U_\infty^{*2}\right)$. From the figure, the increases of the coefficient are mainly due to the interaction between the shock wave and the turbulent boundary layer. The leading shock wave lead to the obvious increase of the skin friction at around $x \in [60, 80]$. Then the coefficient exhibit some decrease ahead of the reflected shock wave at around $x \in [210, 230]$. The shock wave plays as an amplification which apparently promote the intensity of turbulence through the interaction, which is directly reflected in the skin friction.

3.1 Integral analysis

In order to understand the mechanism of the skin friction, a direct connection between the skin friction and flow field is needed. Integral identities are valuable tools for the investigation of wall-bounded flows. By a wall-normal integration, mean-flow quantities varying in the wall-normal direction through the shear layer are reduced to scalar quantities, allowing for a compact characterization of their streamwise evolution. Following the studies of Fukagata *et al.* (2002) and Wenzel *et al.* (2022), we analysis the the behaviour of the $x-$momentum equation by using integral relations for c_f. The average momental equation along x direction can be written as

$$\overline{\rho}\tilde{u}\frac{\partial \tilde{u}}{\partial x} + \overline{\rho}\tilde{v}\frac{\partial \tilde{u}}{\partial y} = -\frac{1}{\gamma M a_\infty^2}\frac{\partial \overline{p}}{\partial x} + \frac{1}{Re}\left[\frac{\partial \overline{\tau}_{xx}}{\partial x} + \frac{\partial \overline{\tau}_{xy}}{\partial y}\right] - \frac{\partial\left(\overline{\rho}\widetilde{u''u''}\right)}{\partial x} - \frac{\partial\left(\overline{\rho}\widetilde{u''v''}\right)}{\partial y} \tag{9}$$

where

$$\overline{\tau}_{xx} = \overline{\mu}\left(\frac{4}{3}\frac{\partial \overline{u}}{\partial x} - \frac{2}{3}\frac{\partial \overline{v}}{\partial y}\right) + \overline{\mu'\left(\frac{4}{3}\frac{\partial u'}{\partial x} - \frac{2}{3}\frac{\partial v'}{\partial y}\right)} \tag{10}$$

$$\overline{\tau}_{xy} = \overline{\mu}\left(\frac{\partial \overline{u}}{\partial y} + \frac{\partial \overline{v}}{\partial x}\right) + \overline{\mu'\left(\frac{\partial u'}{\partial y} + \frac{\partial v'}{\partial x}\right)} \tag{11}$$

$$C_f = \frac{2\overline{\tau}_w}{\rho_\infty u_\infty^2} = \frac{2\overline{\mu}_w}{Re}\frac{\partial \overline{u}}{\partial y}. \tag{12}$$

Hereinafter, for an arbitrary variable f Reynolds (ensemble) averages are denoted by an overbar, $\overline{f}$. The density-weighted Favre averages are denoted by a tilde, $\tilde{f} = \overline{\rho f}/\overline{\rho}$and fluctuations around the Reynolds and Favre averages are denoted by single and double primes, $f' = f - \overline{f}$ and $f'' = f - \tilde{f}$, respectively.

Integration of the equation (9), from the lower surface $y = 0$ of air intake to upper surface $y = y_b$, leads to the following relation

$$\begin{aligned}&\frac{-C_f^{y_b} - C_f^d}{2} = \\ &\frac{1}{Re}\overline{\mu}\frac{\partial \overline{u}}{\partial y}\bigg|_{y=y_b} - \frac{1}{Re}\overline{\mu}\frac{\partial \overline{u}}{\partial y}\bigg|_{y=0} = \\ &\int_0^{y_b}\left[-\frac{1}{\gamma M_e^2}\frac{\partial \overline{p}}{\partial x} + \frac{1}{Re}\frac{\partial \overline{\tau}_{xx}}{\partial x} - \frac{\partial\left(\overline{\rho}\widetilde{u''u''}\right)}{\partial x}\right]dy \\ &-\int_0^{y_b}\overline{\rho}\tilde{u}\frac{\partial \tilde{u}}{\partial x}dy - \int_0^{y_b}\overline{\rho}\tilde{v}\frac{\partial \tilde{u}}{\partial y}dy.\end{aligned} \tag{13}$$

At the same time, twofold repeated integration of the equation (9) lead to

$$\begin{aligned}&\int_0^{y_b}\int_0^{\xi_1}\overline{\rho}\tilde{u}\frac{\partial \tilde{u}}{\partial x} + \overline{\rho}\tilde{v}\frac{\partial \tilde{u}}{\partial y}dyd\xi_1 = \\ &\int_0^{y_b}\int_0^{\xi_1} -\frac{1}{\gamma M a_\infty^2}\frac{\partial \overline{p}}{\partial x} + \frac{1}{Re}\left[\frac{\partial \overline{\tau}_{xx}}{\partial x} + \frac{\partial \overline{\tau}_{xy}}{\partial y}\right] \\ &-\frac{\partial\left(\overline{\rho}\widetilde{u''u''}\right)}{\partial x} - \frac{\partial\left(\overline{\rho}\widetilde{u''v''}\right)}{\partial y}dyd\xi_1.\end{aligned} \tag{14}$$

Equations (13) and (14), together with the Cauchy's formula for n repeated integrations

$$\begin{aligned}&\int_a^{y_b}\int_a^{\xi}\cdots\int_a^{\xi_{n-1}} f(\xi_n)d\xi_n\cdots d\xi_2 d\xi_1 = \\ &\qquad\frac{1}{(n-1)!}\int_a^{y_b}(y_b - y)^{n-1}f(y)dy,\end{aligned} \tag{15}$$

results in a explicit formula for the skin-friction over the lower surface

$$\begin{aligned}C_f^d = &\underbrace{\frac{2}{\mathrm{Re}\, y_b}\int_0^{y_b}\left[\bar{\mu}\frac{\partial \bar{u}}{\partial y} + \bar{\mu}\frac{\partial \bar{v}}{\partial x}\right]\mathrm{d}y}_{c_f^{Me}} + \\ &\underbrace{\frac{2}{\mathrm{Re}\, y_b}\int_0^{y_b}\left[(y - y_b)\overline{\mu'\left(\frac{4}{3}\frac{\partial u'}{\partial x} - \frac{2}{3}\frac{\partial v'}{\partial y}\right)}\right]\mathrm{d}y}_{c_f^V} \\ &\underbrace{-\frac{2}{y_b}\int_0^{y_b}(y_b - y)\left[\tilde{v}\bar{\rho}\frac{\partial \tilde{u}}{\partial y}\right]\mathrm{d}y}_{c_f^{Mc}} \underbrace{-\frac{2}{y_b}\int_0^{y_b}\left[\bar{\rho}\widetilde{u''v''}\right]\mathrm{d}y}_{c_f^{Tc}} + \\ &\underbrace{\frac{2}{y_b}\int_0^{y_b}(y_b - y)\left[-\tilde{u}\bar{\rho}\frac{\partial \tilde{u}}{\partial x} - \frac{\partial \bar{\rho}\widetilde{u''u''}}{\partial x} + \frac{1}{\mathrm{Re}}\frac{\overline{\tau_{xx}}}{\partial x} - \frac{1}{\gamma M_e^2}\frac{\partial \bar{p}}{\partial x}\right]\mathrm{d}y}_{c_f^D},\end{aligned} \tag{16}$$

where C_f^{Me} stands for the mean-flow shear term; C_f^{Mc}, mean-convection term; C_f^{Tc}, turbulent-convection term; C_f^D spatial-development term; C_f^V viscous-stress-fluctuation term.

Figure 3 exhibits the streamwise evolution of skin friction coefficient and each parts based on equation (16) over the lower surface for this air intake. From the decomposition, we can find that turbulence induced drag coefficient $C_f^V + C_f^{Tc}$ is the most dominant and the mean-flow shear induced term C_f^{Me} of the flow field do not have any contribution graphically.

These indicate that the total drag inside the intake are mainly induced by turbulence.

In the inner flow of intake, shockwave turbulent boundary layer interaction also play a very important role. In this case, the interaction do not lead to separation. Furthermore, the shockwave turbulent boundary layer interaction will obviously change the gradients for the variables, which is reflected in the terms of convection C_f^{Mc} and spatial development term C_f^D. Only around the position of interactions, do the amplitudes of convection and development term become large.

4 Conclusion

In this study, direct numerical simulations are performed to understand the mechanism of drag production inside a hypersonic air intake. An integral analysis is performed and it is found that the turbulent induced drag is the dominant for this inner flow. Shockwave turbulent boundary layer interaction acts as an amplifier which obviously enhances the turbulences and then leads to obviously increase of drag.

REFERENCES

Fukagata, Koji, Iwamoto, Kaoru & Kasagi, Nobuhide 2002 Contribution of reynolds stress distribution to the skin friction in wall-bounded flows. *Physics of Fluids* **14** (11), L73–L76.

Li, Xinliang, Fu, Dexun & Ma, Yanwen 2008 Direct numerical simulation of hypersonic boundary layer transition over a blunt cone. *AIAA Journal* **46** (11), 2899–2913.

Li, Xinliang, Fu, Dexun & Ma, Yanwen 2010 Direct numerical simulation of hypersonic boundary layer transition over a blunt cone with a small angle of attack. *Physics of Fluids* **22** (2), 025105.

Liang, Xian, Li, Xinliang, Fu, Dexun & Ma, Yanwen 2010 Effects of wall temperature on boundary layer stability over a blunt cone at mach 7.99. *Computers & Fluids* **39** (2), 359–371.

Paull, A., Stalker, R. J. & Mee, D. J. 1995 Experiments on supersonic combustion ramjet propulsion in a shock tunnel. *Journal of Fluid Mechanics* **296**, 159–183.

Robinson, M. J., Mee, D. J. & Paull, A. 2006 Scramjet lift, thrust and pitching-moment characteristics measured in a shock tunnel. *Journal of Propulsion and Power* **22** (1), 85–95.

Urzay, Javier 2018 Supersonic combustion in air-breathing propulsion systems for hypersonic flight. *Annual Review of Fluid Mechanics* **50** (1), 593–627.

Van Driest, E. R. 1951 Turbulent boundary layer in compressible fluids. *Journal of the Aeronautical Sciences* **18** (3), 145–160.

Wenzel, Christoph, Gibis, Tobias & Kloker, Markus 2022 About the influences of compressibility, heat transfer and pressure gradients in compressible turbulent boundary layers. *Journal of Fluid Mechanics* **930**, A1.

Xi, Youcheng, Ren, Jie & Fu, Song 2021 Hypersonic attachment-line instabilities with large sweep mach numbers. *Journal of Fluid Mechanics* **915**, A44.

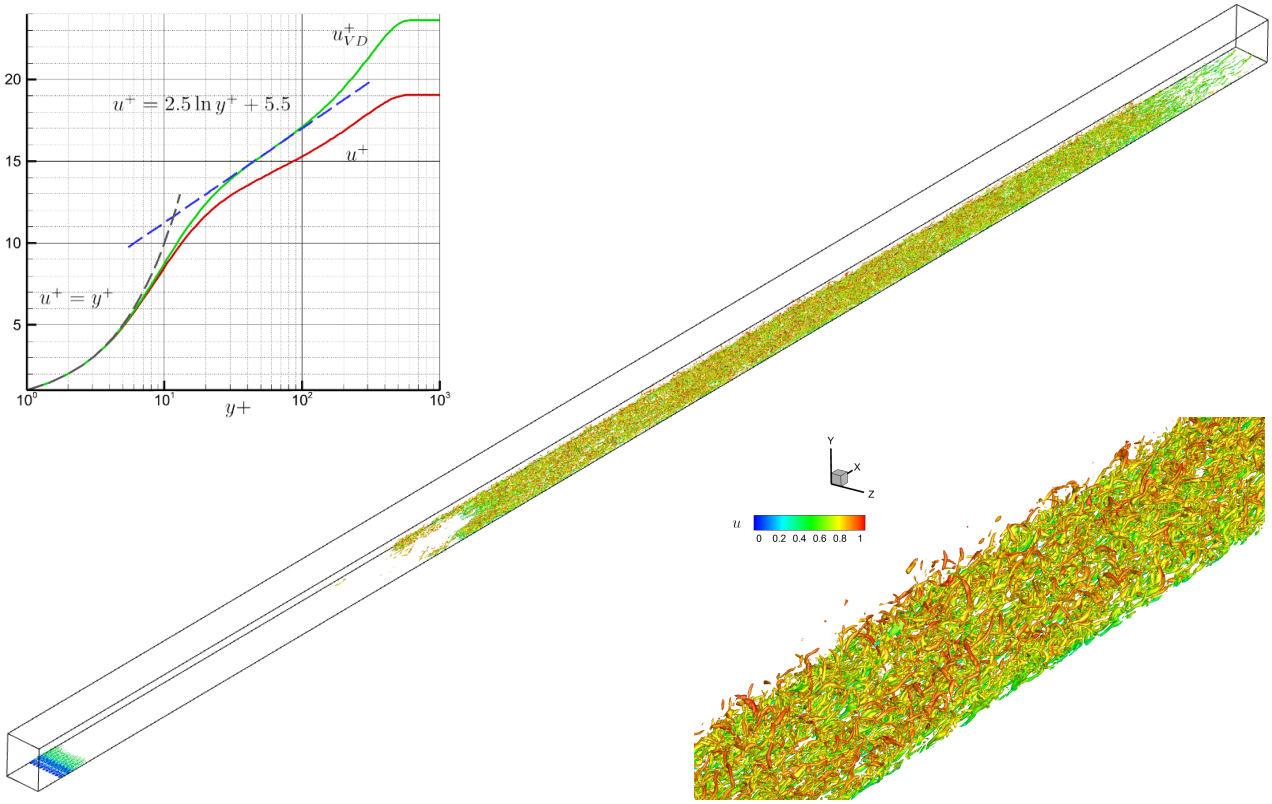

Figure 1. Snapshots of vortices by iso-surface of the λ_2-criterion with $\lambda_2 = -0.05$ for transitional flat boundary layer. The profiles of $u^+ = u/u_\tau$ and $u^+_{VD} = \sqrt{\rho/\rho_w}u^+$ at $x = 1400$ are shown on the top left.

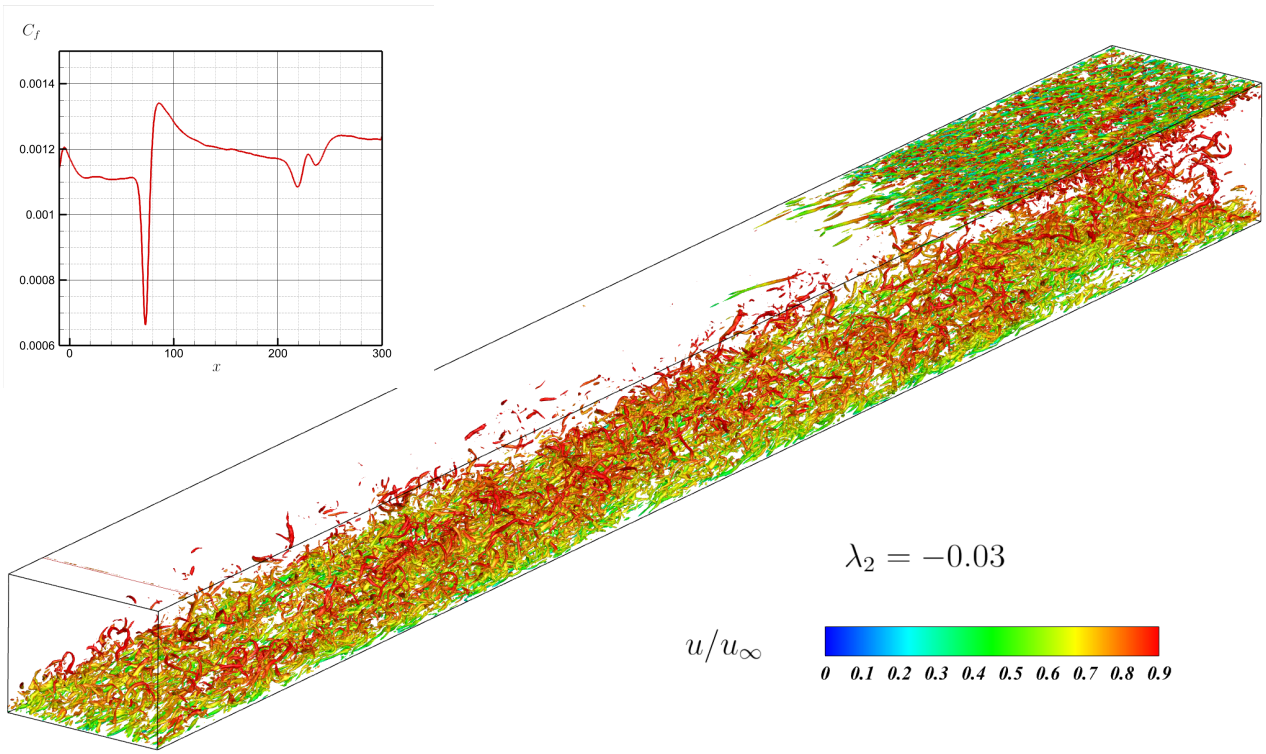

Figure 2. Snapshots of vortices by iso-surface of the λ_2-criterion with $\lambda_2 = -0.03$ for turbulent intake. The average skin-friction coefficient C_f of the lower surface is shown on the top left.

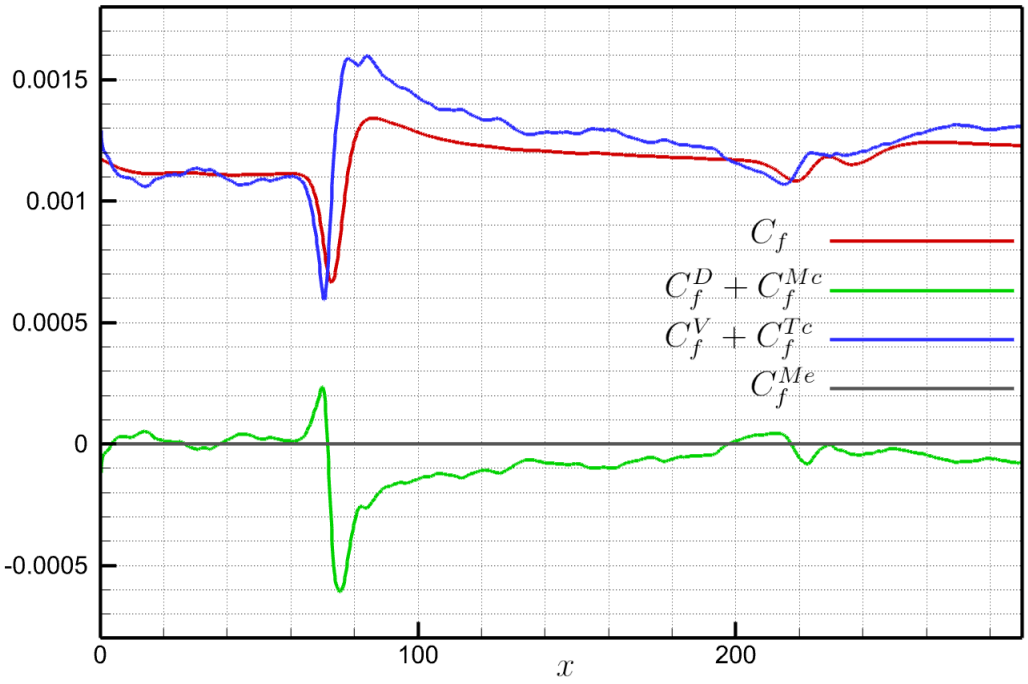

Figure 3. Decomposition of the lower surface skin friction C_f.